



# Time-resolved quantitative inter-eye comparison of cardiac cycle-induced blood volume changes in the human retina

RALF-PETER TORNOW,<sup>1,\*</sup> JAN ODSTRČILIK,<sup>2</sup> AND RADIM KOLAR<sup>2</sup>

<sup>1</sup>*Department of Ophthalmology, Friedrich-Alexander-University of Erlangen-Nuremberg, 91056 Erlangen, Germany*

<sup>2</sup>*Department of Biomedical Engineering, Faculty of Electrical Engineering and Communication, Brno University of Technology, 602 00 Brno, Czech Republic*

\*[ralf.tornow@web.de](mailto:ralf.tornow@web.de)

**Abstract:** We describe a low-cost, easy to use binocular instrument to acquire retinal video sequences of both eyes simultaneously. After image registration, cardiac cycle-induced pulsatile light attenuation changes can be measured quantitatively with high spatial and temporal resolution. Parameters such as amplitude, pulse form, and time shift between light attenuation changes can be calculated and compared between eye sides. Deviation from inter-eye symmetry can be not only an early sign of beginning eye diseases such as glaucoma but also a sign of pathological changes in the carotid arteries; hence, this method can improve the early detection of pathological changes. Important features compared to existing monocular instruments are a narrow band light source with the wavelength close to the peak of the blood extinction, and a proportional relationship of image intensity and light intensity, which are the main requirements for quantitative evaluation.

© 2018 Optical Society of America under the terms of the [OSA Open Access Publishing Agreement](#)

## 1. Introduction

The easily accessible retinal blood vessels, capillaries, and tissue offer possibilities for direct observation and a unique possibility to study vascular, neural, and ophthalmic disorders. Different parameters of the human eye change according to the cardiac cycle, e.g., the intraocular pressure (IOP), eye length, and retinal reflection. The pulsatile changing light reflection is due to the pulsatile changing amount of blood in the retinal tissue and vessels [1–8]. The pulse form and amplitude of the pulsatile changing reflection and the pulsatile changing part of the IOP (ophthalmic pulse amplitude) can be related to different factors, e.g., the IOP [4] and carotid stenosis [5,9].

In early studies describing pulsatile retinal reflection, non-imaging methods were used. Using state of the art CCD and CMOS camera technology, the acquisition of video sequences of the ocular fundus is also possible and adds high spatial resolution to the existing temporal resolution. Retinal video recording and image processing methods have been employed to assess different parameters of the eye, e.g., the reaction of the vessel caliber to flickering light stimulation [10,11], to assess spontaneous venous pulsation [8,12–15], and to measure flickering light-induced reflectance changes of the human papilla and peripapillary region [16].

In the context of early detection of eye diseases, it is interesting that many parameters in glaucoma indicate inter-eye asymmetry. IOP asymmetry is a common finding in patients with glaucoma [17]. Inter-eye macular thickness asymmetry and total retinal nerve fiber layer (RNFL) thickness are also discussed as promising parameters for identifying early primary open-angle glaucoma [18]. De Leon *et al.* [19] reported differences of retinal arterial and venular caliber between both eyes in asymmetric glaucoma and Fansi *et al.* [20] submitted that the rim area to disc area asymmetry ratio (computed from values for the left and right eye) appeared to best distinguish between groups of healthy and three different groups of

glaucoma progression. To compare these slowly changing or constant parameters between the eyes, they can be measured individually. The deviation from symmetry can be an early sign of beginning disease.

However, to compare cardiac cycle-induced fast changing parameters such as pulse form, amplitude, and especially time shift between sides, both eyes must be measured simultaneously. Whereas non-imaging binocular instruments were described in early experiments in photometric studies to measure arm-to-retina circulation times in both eyes simultaneously [1,4,21], simultaneous or binocular acquisition is not possible with the current retinal imaging technologies. Owing to their size, existing monocular imaging instruments cannot be combined to measure both eyes simultaneously.

The parallel video acquisition of both eyes simultaneously can enable the comparison of blood-volume-related parameters between both sides with high temporal and spatial resolution for the detection of deviation from symmetry. As the development of diseases such as glaucoma and carotid stenosis probably differs between sides at the beginning, the detection of any asymmetry could be an opportunity for early diagnosis.

In this paper, we describe an instrument for the acquisition of retinal video sequences of both eyes simultaneously with exact synchronization, a method to quantitatively calculate pulsatile attenuation changes from intensity values with high temporal and spatial resolution, and different examples demonstrating the characteristics of the presented method and possible clinical application.

## 2. Experimental system

There are certain indispensable requirements for such an instrument. First, it must be sufficiently small to allow both eyes to be measured simultaneously. Secondly, for quantitative measurements of the pulsatile attenuation changes, the illumination must be stable over time, and thirdly, there must be a proportional relationship between the light intensity  $I$  in the image plane and the resulting gray value  $GV$  of the image ( $I \propto GV$ ). Further, there should be high contrast for small changes in blood volume, which means the wavelength has to be selected so that the light absorption of blood is high. For stable fixation during the data acquisition, an effective fixation target must be present. Preferably, the instrument should be inexpensive and for a clinical application, it should be easy to use. The main components of the developed instrument and the principle of evaluation are described in the following sections.

### 2.1 Optic design

#### 2.1.1 Imaging

The developed instrument was based on the standard principle of fundus cameras [22]. Figure 1 displays the experimental setup. An ophthalmic lens (40D, Volk Optical Inc, USA) formed an intermediate aerial image of the retina in the image plane R2. This image was reimaged by a lens system (2 achromatic lenses 2 x 120 mm focal length, Qioptiq, Germany) to the sensor plane R3 of a CMOS camera (UI-3060 Rev 2, USB 3.0, IDS Imaging Development Systems GmbH, Germany) with  $1936 \times 1216$  pixels. An area of interest of  $1000 \times 770$  pixels was selected to match the field of view of the camera to formerly used CCD cameras with a smaller sensor [22], without changing the optics. With this setting, one pixel corresponded to 1.2 arcmin of the field of view. To ensure a linear transfer function, gamma was set to "1". The black level was automatically adjusted by the CMOS sensor.

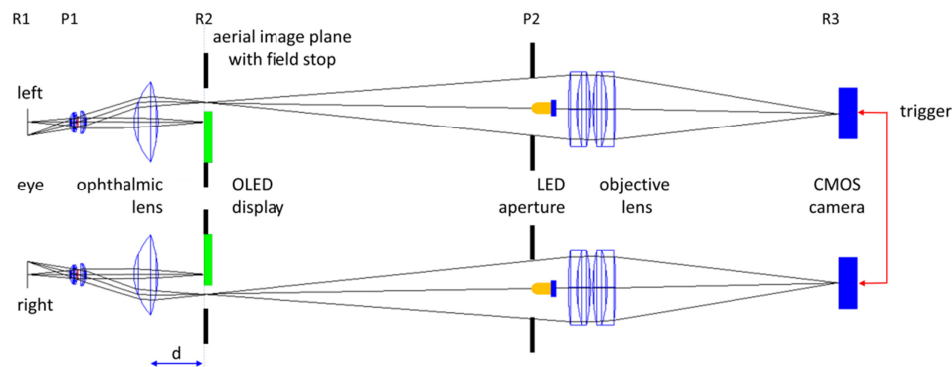


Fig. 1. Setup of binocular video ophthalmoscope (top view). Rx and Px mark retinal (R) and pupillary (P) planes. For a frontal view on the aerial image plane, see Fig. 2. For focusing, distance  $d$  can be changed for each monocular ophthalmoscope separately.

### 2.1.2 Field stop and fixation

As we were mainly interested in optic nerve head (ONH) imaging, a field stop was placed in image plane R2. Only a rectangular area around the image of the ONH could pass this field stop. The field of view was  $20^\circ \times 15^\circ$  with the ONH centered; the central part of the retinal image (fovea) was blocked by this field stop. The light reflected from the ophthalmic lens was also blocked by this field stop. It was necessary to manually align the instrument to the eyes separately (see below) in such a manner that the corneal reflex was also directed outside the retinal image.

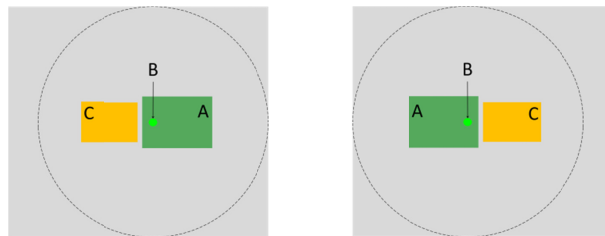


Fig. 2. Frontal view on aerial image plane R2. A: OLED display. B: Fixation target displayed on OLED display. C: Opening in field stop. The subject observes a bright orange field at this position. Dotted circle: Position of ophthalmic lens (not in aerial image plane R2).

An OLED display ( $800 \times 600$  pixels, green light, Olightek, Kunming, China) was fixed in aerial image plane R2 to present a fixation target for the subject to reduce eye movements during video acquisition. When looking into the binocular instrument, the subject could see only the fixation targets and the bright rectangles around the ONH formed by the light used for imaging (see Fig. 2).

### 2.1.3 Illumination

The illumination differed from standard fundus cameras. In conventional fundus cameras, the fundus is illuminated by forming a ring of light on the subjects' cornea with a central area reserved for observation. In the proposed approach, the exit and entrance pupils were inverted: the central area of the pupil was used for illumination (entrance pupil) and the remainder of the pupil was used for imaging (exit pupil). This configuration corresponds to the configuration of the entrance and exit pupil used in scanning laser ophthalmoscopy. Owing to this pupil configuration, the light source was realized simply, no ring forming optics or mirrors were necessary. An LED (577 nm, 15 nm FWHM, 5 mm diameter, constant current power supply) was placed in the conjugate plane of the pupil (P2) centered on the

optical axis, shining the light towards the eye. Because of the pupil magnification (pupil plane P1 / conjugate pupil plane P2) of the system, the image of the LED in pupil plane P1 of the subject was reduced to 1 mm. A circular aperture was placed in pupil plane P2, close to the LED, that acted as the aperture stop of the optical system.

Figure 3 displays the spectral distribution of the LED light accompanied by the attenuation of a 1- $\mu\text{m}$  thick blood layer. The attenuation coefficient  $\mu_{\text{eff}}(\lambda)$  of blood (including absorption and scattering) was calculated using the absorption and scattering coefficients and the scattering anisotropy coefficient according to [23]. The peak of the LED light coincides with the peak in the light absorption of blood resulting in high contrast for small changes in blood volume. For comparison, the relative sensitivity spectrum of the green channel of a digital SLR camera is also included.

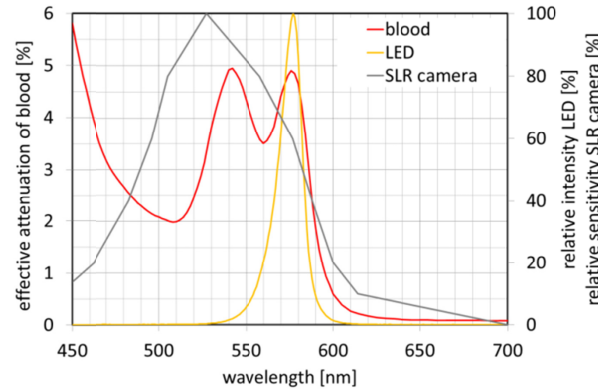


Fig. 3. Relative intensity spectrum of LED light, relative sensitivity spectrum of the green channel of a digital SLR camera, and spectrum of effective attenuation of a 1- $\mu\text{m}$  (single path) thick blood layer (100% oxygen saturation).

The improvement in light attenuation, caused by a thin blood layer, of the proposed system (with an LED as light source), compared to a standard fundus camera (with a tungsten lamp as light source, and the green channel of a digital SLR camera as detector), can be estimated using the spectral distribution of the intensity of the light source  $I(\lambda)$ , reflection of the ocular fundus  $R(\lambda)$ , spectral sensitivity of the detector  $S(\lambda)$ , and effective attenuation coefficient  $\mu_{\text{eff}}(\lambda)$  of blood according to Eq. (1):

$$\text{light attenuation} = \frac{\int_{450}^{700} I(\lambda) * R(\lambda) * S(\lambda) * \mu_{\text{eff}}(\lambda) * d * d\lambda}{\int_{450}^{700} I(\lambda) * R(\lambda) * S(\lambda) * d\lambda} \quad (1)$$

The spectral distribution of the light sources were measured using a spectral radiometer (CAS 140 CT, Instrument Systems, Germany), the reflection of the fundus was acquired from Delori [24], the sensitivity of the SLR camera from [25], and of the CMOS camera from the data sheet. A blood layer with a thickness of  $d = 1 \mu\text{m}$  reduced the light intensity by 4.1% in the proposed instrument, compared to 2.6% using a standard fundus camera, corresponding to an improvement of 60%.

The video sequences were recorded with a power of 12  $\mu\text{W}$  in the pupil plane P1 (at approximately 20 mA LED current) resulting in a retinal illumination of 30  $\mu\text{W}/\text{cm}^2$  on the retina (assuming a transmission of the cornea and lens of “1”). This value is significantly below the MPE value of 220  $\mu\text{W}/\text{cm}^2$  for long exposures [26].

#### 2.1.4 Mechanical construction/setup

The ophthalmoscopes were mounted using Microbench and Tube System components (Qioptiq, Germany). For focusing, the distance  $d$  (Fig. 1) between the ophthalmic lens and the



retinal plane R2 could be changed by motor driven z translation stages. The size of one ophthalmoscope was approximately  $6 \times 6 \times 35 \text{ cm}^3$ , which is sufficiently small to place an ophthalmoscope in front of each eye. For alignment to the eyes, the ophthalmoscopes were attached to two independent slit lamp XYZ mounts.

## 2.2 Software and measurements

### 2.2.1 Data acquisition

To ensure exact synchronization of the corresponding images of the video sequences, a hardware trigger for the cameras was employed [27]. Data acquisition software was developed to select the parameters of the cameras (frame rate, exposure time, gain), to move the position of the fixation targets on the OLED displays (to be able to direct the patients viewing direction), and to display live images of both cameras on the screen of a laptop. The data acquisition software executed on an HP ZBook 14 G2. During data acquisition, the time stamp was written to each frame (with millisecond resolution) indicating the moment of image capture by each camera to allow verification synchronization offline.

### 2.2.2 Image registration

Despite the use of fixation targets, the acquired video sequences indicated eye movements. To compensate for these eye movements, the video sequences were registered offline using a two-step process using the first frame of the sequence as a reference [28]. In the first stage, large movements were corrected via phase correlation, employing a Fourier shift theorem for the estimation of large inter-frame translation. The Lucas-Kanade [29] approach was used in the second stage of registration process to increase its precision. The tracking points were detected on a vascular tree, which was segmented using eigenvalues of the Hessian matrix of the pixel's neighborhood and Otsu thresholding. Small, segmented regions were consequently removed as we assumed that segmented blood vessels create longer structures. Finally, binary skeletonization was used to obtain the points on the vessel centerlines, which were used for tracking. The basic optical flow approach [29] was used for estimation of the global Euclidean transformation matrix for each frame  $n$ , employing translation and rotation. The final values of translations ( $\Delta x_n$ ,  $\Delta y_n$ ) and rotations ( $\Delta \phi_n$ ) were computed for each frame by merging the data from both stages. These extracted signals were then used for the frame registration. Other applications are possible, e.g., eye fixation analysis [30].

### 2.2.3 Measurements

The study followed the tenets of the declaration of Helsinki for research involving human subjects and informed consent was obtained from all participants of the study. The clinical application of the method was performed in the framework of the Erlangen Glaucoma Registry (EGR), a clinical registry (ClinicalTrials.gov identifier: NCT00494923) for cross sectional and longitudinal observation of patients with open-angle glaucoma or glaucoma suspect, founded in 1991 [31].

Short video sequences of 10 s duration were captured from the ONH of subjects with dilated pupils. The video ophthalmoscope does function with undilated pupils with a minimum pupil diameter of approximately 2 mm. However, the subjects discussed herein were measured with dilated pupils owing to the order of the other clinical investigations. Furthermore, dilated pupils decrease the diameter fluctuations (and consequently intensity changes) during the acquisition and increase the range of tolerable eye movements without disturbing reflection and scattering from the pupil edge. First, the right instrument was aligned to the eye such that a clear image of the ONH was visible on the screen and reflections were removed or minimized by small XYZ movements of the instrument. Then, the subject was asked to maintain fixation, and the left eye was aligned in the same manner.

Finally, the video acquisition was initiated. Normally, the alignment procedure required less than 20 s. After registration of the video sequences, different parameters were calculated.

### 2.3 Calculating absorption changes from intensity changes

For consistency of formulae and results, in the following descriptions and graphs, the time is expressed as frame number  $n$ . All video sequences were acquired with a frame rate of 25 fps and an exposure time of 39 ms.

#### 2.3.1 Pulsatile attenuation changes

The temporal variation of the intensity  $I(n)$  can be evaluated offline at any area of interest (AOI) within the field of view of the registered video sequences.

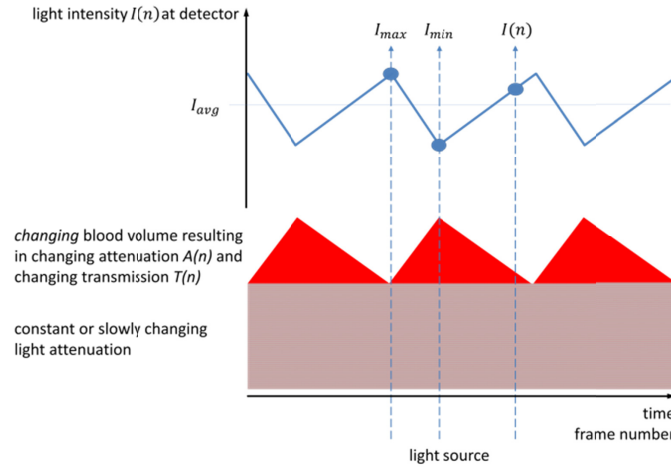


Fig. 4. Schematic representation of relationship between changing attenuation / blood volume and changing light intensity. Reddish part represents constant light absorption and red layer represents the *changing* part of the blood volume. High blood volume results in low intensity and vice versa.

Although there could be different reasons for cardiac cycle-induced attenuation changes (see Discussion), the calculation presented herein is based on the light attenuation (including absorption and scattering) by a thin blood layer. The light intensity  $I(n)$  at the detector and resulting gray value of the image depend on two components: a constant component that is determined by the parameters of the instrument (light intensity of the LED, detector gain, apertures) and the eye (transmission, pupil size, absorption of the different layers and pigments, reflection of the retina), and a second component that is modulated by the *changing* part of the blood volume according to the cardiac cycle. Assuming constant illumination  $I_0$  and stable fixation and alignment [32] of the instrument, the light intensity at the detector is proportional to the light reflected from the ocular fundus. Increasing blood volume results in decreasing intensity and vice versa (see Fig. 4). Hence, the light absorption of the *changing* part of the blood volume can be calculated directly from the intensity values without additional assumption, based only on the general definition of transmission  $T = I/I_0$ . The maximum intensity during one heartbeat is  $I_{max}$  at the beginning of the heartbeat (lowest blood volume, see Fig. 4). During the heartbeat, the intensity  $I(n)$  decreases owing to the increasing blood volume resulting in decreasing transmission and increasing absorption. The transmission  $T(n)$  of the *changing* part of the blood layer is

$$T(n) = \frac{I(n)}{I_{max}} \quad (2)$$

resulting in an attenuation  $A(n)$  of the *changing* part of the blood layer (assuming  $T + A = 1$ )

$$A(n) = 1 - T(n) = 1 - \frac{I(n)}{I_{max}} \quad (3)$$

The calculated attenuation  $A(n)$  of the *changing* blood layer is independent of the constant parameters of the eye and the instrument (light intensity, camera gain, pupil size, fundus reflection) because changing intensity conditions influence both  $I(n)$  and  $I_{max}$ . An essential condition for the validity of this equation for the resulting gray values of the images is a proportional relationship between the light intensity  $I$  in the image plane and the resulting gray value  $GV$  of the image ( $I \propto GV$ ).

### 2.3.2 Pulsatile attenuation amplitude (PAA)

The pulsatile attenuation amplitude  $PAA$  representing the maximum change in attenuation  $A_{max}$  during one heartbeat can be calculated from Eq. (3) with  $I(n) = I_{min}$

$$PAA = A_{max} = 1 - \frac{I_{min}}{I_{max}} \quad (4)$$

Equation (4) can also be applied to each pixel of a sequence of frames of an entire heartbeat such that the spatial distribution of  $PAA(x,y)$  can be calculated (see Fig. 6). The presented  $PAA$  spatial distribution was calculated for five pulses and the resulting images  $PAA(x,y)$  were averaged.

### 2.3.3 Trend correction

If an entire sequence (250 frames, approximately 10 heartbeats) is examined, the constant part of the light intensity could change slowly owing to small eye movements and loss of optimal alignment. Furthermore, the individual heartbeats are not identical and could have marginally different amplitude such that it is not useful to use the maximum value of a single heartbeat as reference, as in Eq. (3). In this case, the trend signal  $I_{avg}(n)$  of the signal  $I(n)$  is calculated by

$$I_{avg}(n) = \sum_{m=n-12}^{m=n+12} \frac{I(m)}{25} \quad (5)$$

The changing transmission  $T_{trend}(n)$  compared to this trend signal is calculated with

$$T_{trend}(n) = \frac{I(n)}{I_{avg}(n)} \quad (6)$$

resulting in the attenuation

$$A_{trend}(n) = 1 - T_{trend}(n) = 1 - \frac{I(n)}{I_{avg}(n)} \quad (7)$$

### 2.3.4 Presentation of the results

All results are displayed in the diagrams in the following manner. The reference value is either the value at the beginning of a heartbeat ( $I_{max}$ ) or the average value ( $I_{avg}$ ) according to Eq. (3) and Eq. (7), respectively. To avoid negative values and to display the distribution of  $PAA(x,y)$  as an image or a video sequence, the value “100” was added to all results. Hence, the reference value is “100” and a value of “105” indicates a change (increase) of attenuation of 5% and “95” a decrease of 5%. [Visualization 3](#) (Fig. 9) presents, as an example, a video sequence with calculated  $PAA(x,y,n)$  values for one pulse. In this case, the reference value is the beginning of the heartbeat at Frame 3 of the video sequence. This video sequence can thus

be directly analyzed quantitatively at any area of interest using appropriate software (e.g., the live z-profile of ImageJ). To compare the pulse form between sides, the pulses can also be normalized to their minimum and maximum. If pulses are averaged, the standard deviation is displayed in the diagram. Patient data are covered by gray rectangles in the upper left corner of the images and video sequences.

### 3. Results

This section describes the evaluation of a typical measurement and includes specific cases that demonstrate the potential of the proposed instrument. However, the results displayed herein do not yet allow conclusions concerning the correlation of calculated parameters and diseases. Table 1 lists the clinical data of the subjects (peripapillary retinal nerve fiber layer (RNFL) thickness, IOP, and diagnosis). All subjects had clear media. For details on the clinical measurements see [32] and [33].

**Table 1. Patient data**

Subject displayed in	RNFL thickness [ $\mu\text{m}$ ] Right/Left	IOP [mmHg] Right/Left	Diagnosis
Figure 5	63/60	14/16	Glaucoma
Figure 6(A) and Fig. 7	95/90	15/15	No eye disease
Figure 6(B)	92/59	16/14	Glaucoma left eye
Figure 6(C) and Fig. 8	97/94	12/12	No eye disease, macroangiopathy and plaque of the carotid communis on both sides
Figure 9	71/74	11/11	Glaucoma
Figure 10	74/55	16/14	Glaucoma

#### 3.1 Evaluation of typical video sequences

Figure 5 displays a typical recording of 10 s (250 frames). The right eye is presented on the left side and the left eye on the right side (corresponding to the convention in ophthalmology). The average frames of both eyes of the registered video sequences are displayed in Fig. 5(A) (see [Visualization 1](#)) along with two selected AOIs. The intensity in these AOIs is indicated in Fig. 5(B) with the calculated trend signals  $I_{\text{avg}}(n)$  (black lines). There is a small change of the average intensity during the first 75 frames. The cardiac cycle-induced intensity changes can be clearly observed. The calculated change of attenuation is indicated in Fig. 5(C), and Fig. 5(D) displays the calculated distribution of the pulsatile absorption amplitude  $PAA(x,y)$ .

The PAA in the selected AOI is approximately 8% ( $\pm 4\%$ ); it changes to a small amount from pulse to pulse. The increasing edges of the pulses are considerably similar between both sides. The  $PAA(x,y)$  indicates a high value at the neuroretinal rim and also at and beside the vessels (see below).

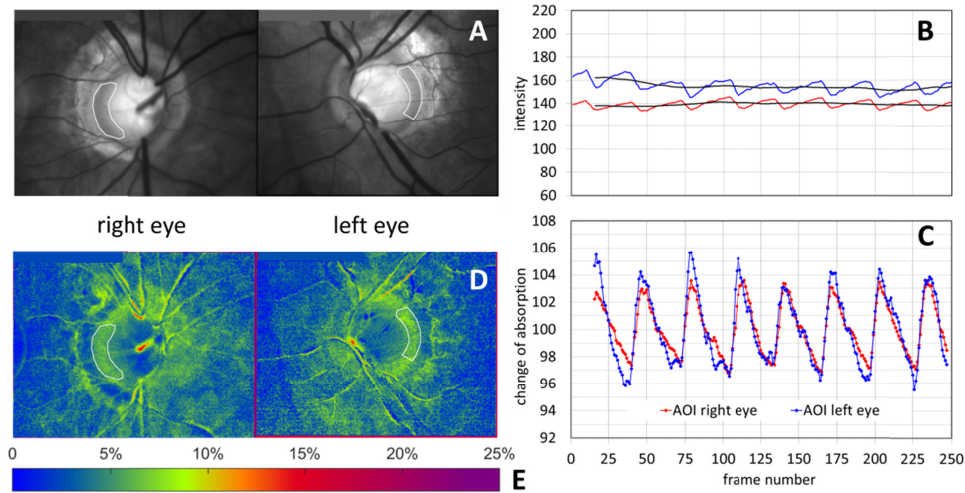


Fig. 5. Evaluation of entire video sequence (10 s, 250 frames) (see [Visualization 1](#), five heartbeats, Frames 72–227). (A): Average frames of right and left eye of entire sequence displaying selected AOIs. (B): Intensity in selected AOIs and calculated trend  $I_{avg}(n)$  (black lines). (C): Change of attenuation calculated according to Eq. (7). (D): Color-coded pulsatile absorption amplitude  $PAA(x,y)$  with selected AOIs.

### 3.2 Spatial distribution of the pulsatile attenuation amplitude $PAA(x,y)$

As indicated in Fig. 5, the distribution of the  $PAA(x,y)$  is a useful tool to compare spatial distribution and inter-eye differences in PAA at a glance. Figure 6 displays the  $PAA(x,y)$  for three subjects for both eyes, Fig. 6(A) is a normal subject without any eye disease, Fig. 6(B) is a glaucoma patient with reduced RNFL thickness on the left side, and Fig. 6(C) is a subject without any eye disease, however macroangiopathy and plaque of the carotid communis on both sides. Areas with high PAA at the neuroretinal rim and on the vessels are clearly visible and the eye sides can be easily compared. Moreover, positions on the retinal vessels with high PAA can be recognized for further evaluation.

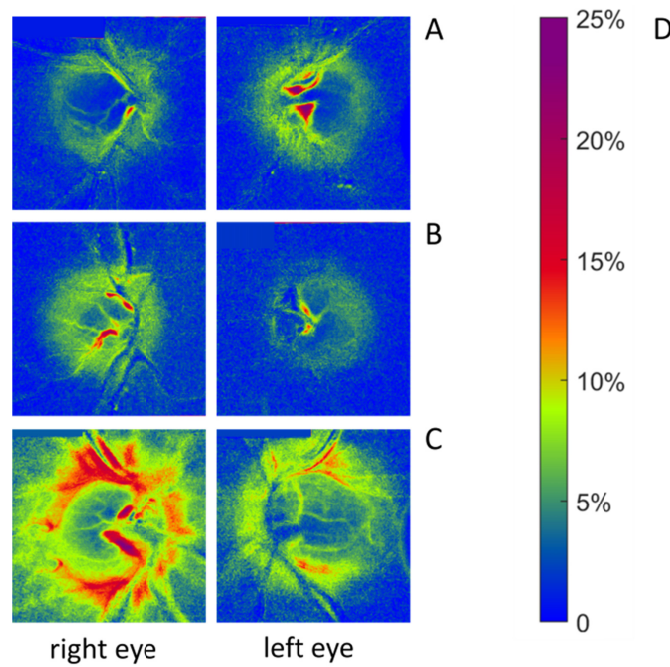


Fig. 6. Distribution of pulsatile absorption amplitude  $PAA(x,y)$  of both eyes for three subjects. (A): Normal subject without eye disease. (B): Patient with glaucoma on left eye. (C): Patient with macroangiopathy and plaque of the carotid communis on both sides. The temporal changes of attenuation for the subjects displayed in (A) and (C) are presented in Fig. 7 and Fig. 8, respectively. (D): Color scale.

The normal subject (Fig. 6(A)) demonstrates similar values on both sides at the neuroretinal rim whereas the subject with glaucoma (Fig. 6(B)) displays reduced values at the left eye. The subject with macroangiopathy and plaque of the carotid communis (Fig. 6(C)) indicate differences between the eyes. A striking effect is the high PAA outside the ONH in the right eye. The temporal change in attenuation  $A(n)$  for the subjects displayed in Fig. 6(A) and Fig. 6(C) are presented in Fig. 7 and Fig. 8, respectively.



### 3.3 Normal subject

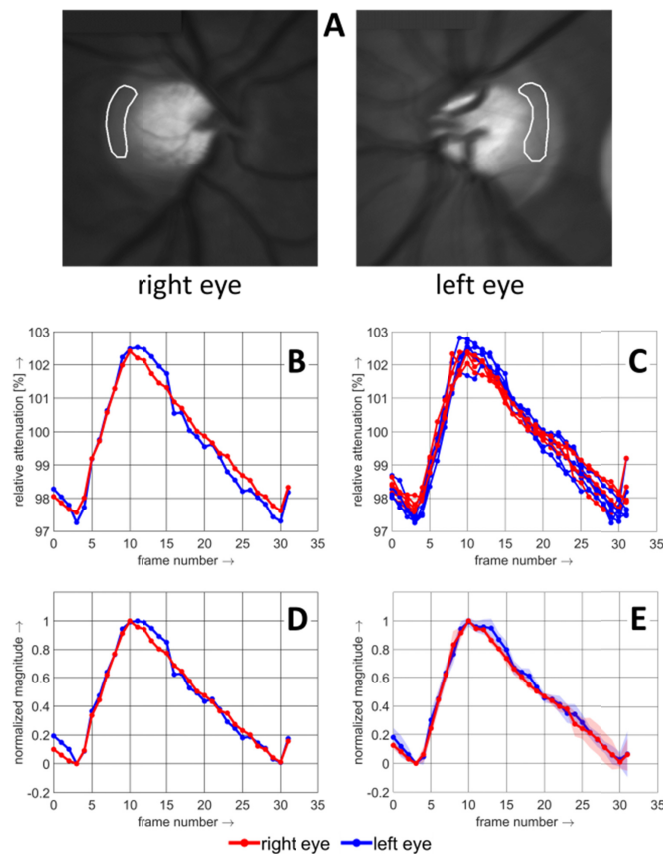


Fig. 7. Subject with no eye disease (corresponding  $PAA(x,y)$  of this subject is displayed in Fig. 6(A)) (A): Average frames of entire sequence indicating AOIs. (B): Change of attenuation  $A(n)$  in AOs for one heartbeat. (C): Five individual pulses. (D): Normalized single pulse (displayed in (B)). (E): Median value of five normalized pulses (displayed in (C)) including standard deviation (bluish and reddish area).

Figure 7 displays the subject with no eye disease from Fig. 6(A). AOIs were selected on the neuroretinal rim. In this case, the single pulses from the right and left eyes are similar in amplitude (Fig. 7(B)) and in normalized pulse form (Fig. 7(D)). The pulses are also relatively stable over time as indicated in Fig. 7(C) for five pulses. Figure 7(D) displays the median of these five pulses with the standard deviation (bluish and reddish area). The increasing parts of the five pulses have small standard deviation (SD), whereas this is higher at the end of the decreasing part of the pulses.

### 3.4 Time delay between the eyes

Figure 8 displays the subject with macroangiopathy and plaque of the carotid communis from Fig. 6(C) in the same manner as the normal subject in Fig. 7. In this case, the single pulses from the right and left eyes differ in amplitude (Fig. 8(B)) and in pulse shape (Fig. 8(D)). The increasing parts of the pulses indicate a marginal time shift of approximately one frame (40 ms) between the eyes and the descending part indicates differences between the eyes. Whereas it is relatively flat for the right eye, it indicates higher variation for the left eye. The five individual pulses for both eyes displayed in Fig. 8(C) are more stable for the right eye

compared to the left eye, which can also be observed in the median pulses and the SD displayed in Fig. 8(E).

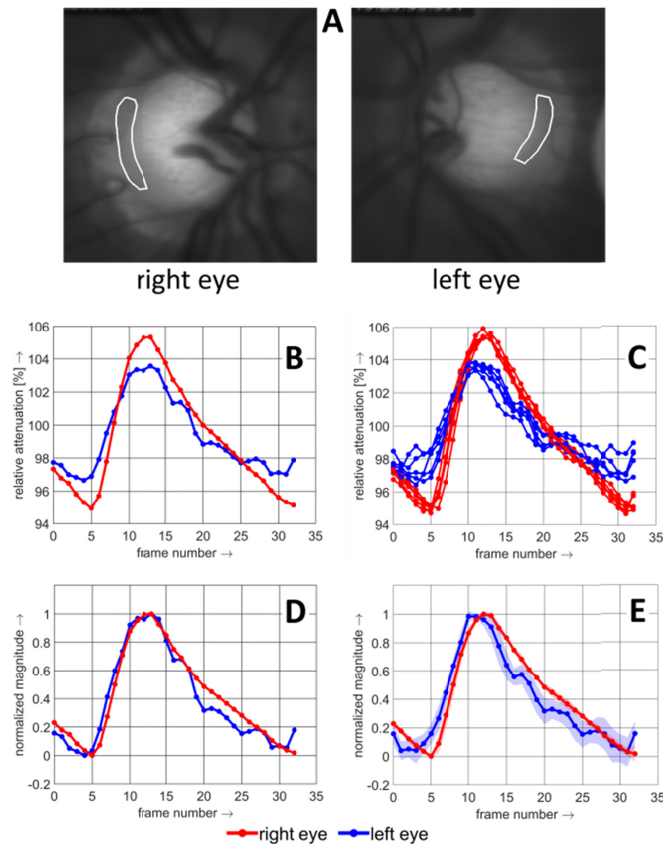


Fig. 8. Subject with no eye disease, however with macroangiopathy and plaque of the carotid communis on both sides (corresponding  $PAA(x,y)$  of this subject is displayed in Fig. 6 (C)). (A): Average frames of entire sequence displaying AOIs. (B): Change of attenuation  $A(n)$  in AOIs for one heartbeat. (C): Five individual pulses. (D): Normalized single pulses (displayed in (B)). (E): Median value of five normalized pulses including standard deviation (bluish and reddish area). A time shift between both sides is clearly visible.

### 3.5 Comparison of attenuation changes between different positions and both eyes

The spatial distribution of  $PAA(x,y)$  allows locating areas with high PAA, and positions to analyze the temporal change in absorption  $A(n)$  can be selected. Figure 9 displays the comparison of attenuation changes between different positions and both eyes. Corresponding AOIs were selected at the entire ONH and on small areas on retinal veins immediately after bifurcations of the vessels. The spontaneous vein pulsation can be observed in this sequence. Average frames of the selected video sequence and the spatial distribution of the pulsatile absorption amplitude  $PAA(x,y)$  are displayed in Fig. 9(A) and Fig. 9(B), respectively. The amplitudes at the ONH are similar between the eyes; however, the small AOIs on the veins immediately after a bifurcation indicate considerable higher attenuation changes than the ONH. To compare the pulse form, normalized single pulses are displayed in Fig. 9(D). There is high agreement in the pulse form for corresponding areas for both eyes, especially at the increasing part of the pulses, however the pulse form at the different positions within the eyes differ. The increasing part at the vessels is delayed compared to the ONH by approximately

two frames (80 ms). The median (including SD) of five individual pulses for each AOI (Fig. 9(E) and Fig. 9(F)) indicate high stability of the pulses in this case.

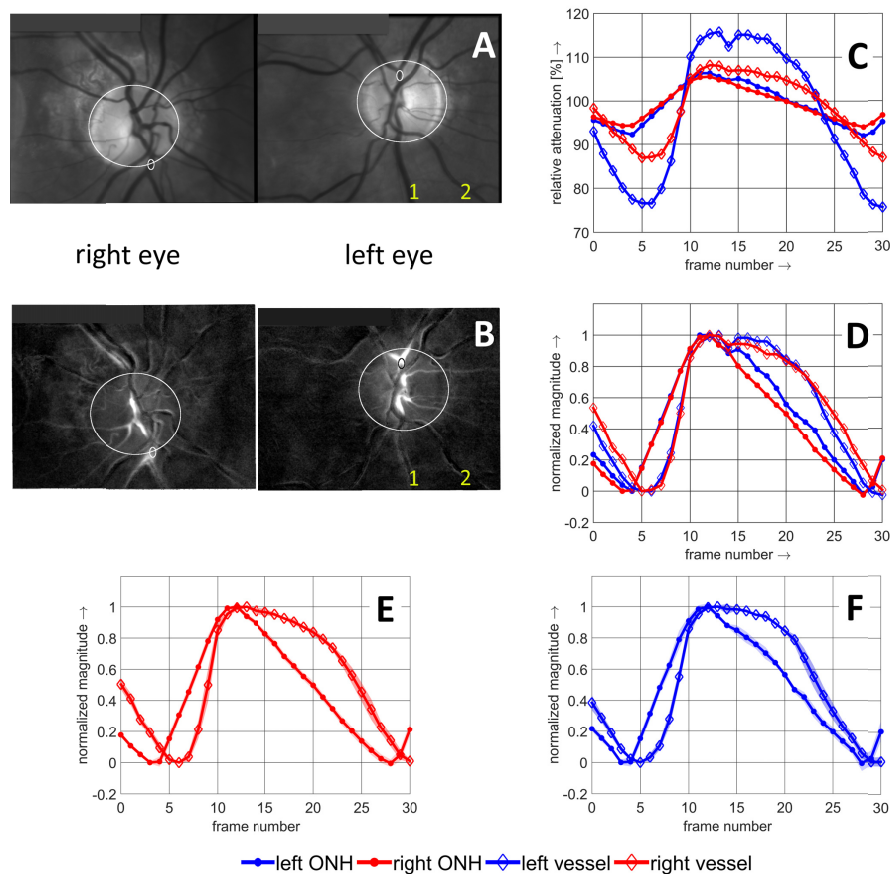


Fig. 9. Comparison of attenuation changes between different positions and both eyes. (A): Average frames of selected video sequence (30 frames) (Visualization 2) displaying selected AOIs (circles, ovals). (B): Spatial distribution of pulsatile absorption amplitude  $PAA(x,y)$  displayed in gray scale without color coding. (C): Change of attenuation  $A(n)$  in AOIs for one heartbeat. (D): Normalized change in intensity  $A(n)$  in AOIs. (E) and (F) display the median of five normalized pulses for the right and left eye, respectively, including standard deviation (bluish and reddish area). Visualization 2 display a changing vessel caliber (Vessel 1) and bending vessel (Vessel 2). Visualization 3 displays the spatial distribution  $A(x,y,n)$  of one heartbeat as a video sequence with Frame 3 as a reference.

### 3.6 Skipped heartbeat

Figure 10 displays the recording of five heartbeats of a subject with one skipped heartbeat without systole. Figure 10(A) displays the average frame of the entire selected sequence (119 frames) with selected AOIs, Fig. 10(B) the change of attenuation in the AOIs, and Fig. 10(C) all color-coded frames  $A(x,y,n)$  of both eyes of the entire sequence. The color coding is modified compared to the color coding in the other Figs. Red represents higher blood volume and blue corresponds to reduced blood volume compared to reference Frame 1. The skipped heartbeat causes a significant blood volume decrease (approximately 8%) between Frames 50 and 75 in both eyes compared to normal values at the beginning of a heartbeat.

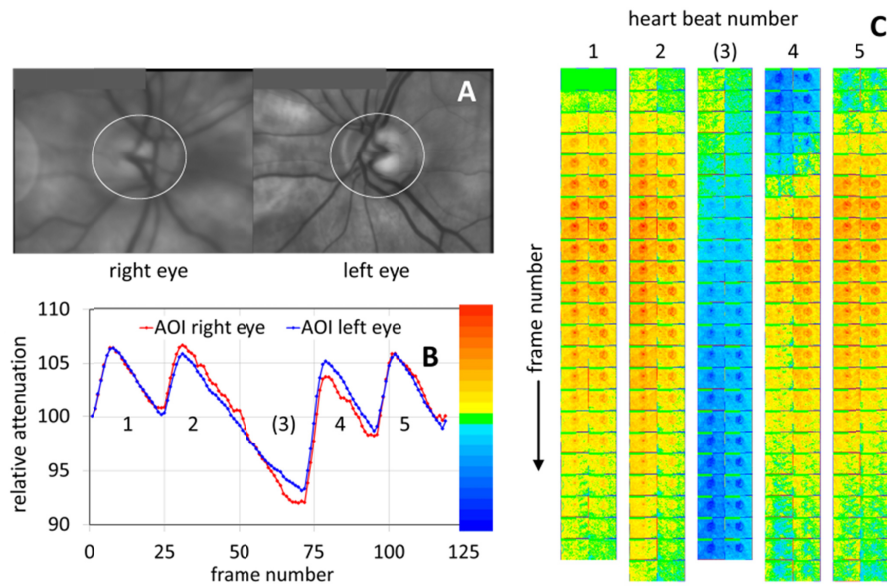


Fig. 10. Patient with skipped heartbeat. (A): Average frame of entire selected sequence (119 frames) with AOIs. (B): Change of absorption  $A(n)$  in selected AOIs (with color bar on the right axis). Reference value is the beginning of the first heartbeat in this sequence (Frame 1). (C): Color coded  $PAA(x,y,n)$  of both eyes of the entire sequence. Red indicates greater blood volume and blue less blood volume compared to the first frame (reference value “100” corresponds to the green color). The starting position of the (skipped) heartbeat (3) is estimated from the heartrate.

#### 4. Discussion

The developed instrument allows the measurement of cardiac cycle-induced light attenuation changes of both eyes simultaneously with high spatial and temporal resolution.

There are different reasons for pulsatile cardiac cycle-induced attenuation changes. One reason is the changing blood volume with resulting changes in absorption and scattering of light. Recently, in the application of imaging photo plethysmography on the skin [34], it has been demonstrated that the reflected light intensity is modulated owing to changes of both scattering and absorption coefficients. These are proportional to the degree of the capillary compression, which occurs owing to artery pulsation.

Figure 6(A) and Fig. 6(B) display the spatial distribution of  $PAA(x,y)$  for a healthy (A) and glaucoma subject (B) with reduced RNFL on the left eye. AOIs are placed on the neuroretinal rim with small capillaries supplying the nerve tissue. Therefore, pulsatile intensity changes related to blood effective attenuation are expected in this region. The PAA magnitudes indicate reduction on the neuroretinal rim for the glaucomatous left eye. A limited number of authors have published that a statistically significant correlation exists between the RNFL thickness and other parameters related to retinal capillaries, particularly radial peripapillary capillary density examined by OCT angiography inside and around the ONH, e.g [35,36]. The positive correlation between blood flow velocity (determined by laser speckle flowgraphy as *mean blur rate* parameter) and RNFL thickness has also been described, e.g [37,38]. The PAA reduction is linked to a reduction of the blood volume absorption, which is in accordance with capillary density reduction and blood flow reduction. The example with a skipped heartbeat (Fig. 10) also demonstrates decreasing relative attenuation that could be explained by diastolic blood outflow resulting in decreasing blood volume during the skipped heartbeat.

However, there are also other reasons for cardiac cycle induced light attenuation changes. It was shown that there is high directionality of tissue scattering, e.g. from the retinal nerve

fiber layer [39–41]. Using high-speed spectral domain optical coherence tomography, An *et al.* [42] found that the ONH experiences continuous oscillatory axial motion that is strongly correlated with simultaneously measured pulsatile blood flow in the central retinal artery. The amplitude of the ONH movement was approximately 4  $\mu\text{m}$ . The increase of retinal thickness caused by expansion of the retinal vessels is in the range of 1  $\mu\text{m}$  as measured by Spahr *et al.* using phase-sensitive full-field swept-source optical coherence tomography [43]. Schmetterer *et al.* [44] investigated the distribution of fundus pulsation amplitude in a region of  $-15^\circ$  to  $+15^\circ$  around the macula using a laser interferometric method. The average fundus pulsation amplitude in the ONH was approximately 10  $\mu\text{m}$ .

These cardiac cycle induced sample movements in conjunction with the directionality of the tissue scattering could result in cardiac cycle induced intensity changes. Additionally, changes in scattering due to changes of orientation of blood constituents (e.g. red blood cells) over the cardiac cycle could also result in intensity changes.

Further work is necessary to clarify the contribution of the different effects described here on the origin of the cardiac cycle induced attenuation changes.

Changing attenuation due to the pulsation of large retinal blood vessels and even small vessels, which are visible owing to their changing blood volume or their movement, can also be observed. This is documented in Fig. 9. If the vessel diameter changes according to the cardiac cycle, there are areas with high PAA along the vessels. This is caused by the fact that the vessels are darker than the background and positions near the vessels have high reflection when the vessel caliber is small (at the beginning of the heartbeat) and become darker when the vessel caliber increases (at the peak of the heartbeat). This can be observed in the vein depicted as Vessel 1 in Fig. 9. In this case, the vein exhibits large diameter pulsation causing PAA changes around the vein.

Furthermore, vessels that bend and change their position, to a small degree, based on the cardiac cycle also change the image intensity and values of  $PAA(x,y)$  at corresponding locations. Reduced  $PAA(x,y)$  values result in areas where the vessels are located at the beginning of the heartbeat and high values where they are located at the peak of a heartbeat. This can be observed in Vessel 2 in Fig. 9(B) and the corresponding video sequence ([Visualization 2](#)). Whereas these results can help to locate moving vessels, it must be noted that precise image registration is necessary for this evaluation; otherwise, artifacts are created. Although in many cases the registration provides satisfactory results, other cases could fail for specific frames (due to eye movement, saccades, and blinking) [28]. The amount of vessel movement and pulsation has been observed as being highly variable among subjects. Two examples presented herein demonstrate a significant amount of vessel movement in [Visualization 2](#), yet only minimal movement in [Visualization 1](#).

Beyond the evaluation of PAA, the time shift of pulse parameters (i.e., the position of minima or maxima) between sides could be an important parameter to detect deviation from normal values due to beginning diseases. For the subject with macroangiopathy and plaque of the carotid communis displayed in Fig. 8, a time shift of pulse parameters between sides can be clearly observed. Carotid atherosclerosis could cause different ocular symptoms [45] and carotid stenosis has been proven to influence the arm to retina circulation time (ARCT), particularly ARCT delay, disparity of ARCT between the eyes, and delayed ciliary circulation at the optic disc [46]. As the level of carotid stenosis is not symmetric, it leads to an impaired blood flow in the ophthalmic artery and the posterior ciliary arteries causing differences in ocular pulse amplitude [3] and possibly differences in dynamic patterns in corresponding retina.

Another noticeable time shift was observed between  $A(n)$  of the entire ONH and the small AOIs placed on retinal veins (Fig. 9). We found these delays to be in the range of 2–3 frames, corresponding to 80 ms to 120 ms. Similar delays regarding the spontaneous vein pulsation phase following the arterial phase have been described in Morgan *et al.* [12] and Moret *et al.* [47].



The assumed time shift indicated in Fig. 8 is in the range of one frame. To better detect a time shift, the temporal resolution of the instrument could be improved by increasing the frame rate and reducing exposure time. In this case, the light intensity also must be increased. This can be increased up to a factor of “7” without leaving the safety range of retinal illumination for unlimited exposure.

Compared to existing (monocular) video ophthalmoscopes that are based on (modified) standard fundus cameras or slit lamps with digital SLR (single-lens reflex) cameras (e.g., Canon, Nikon) as the image detector and tungsten halogen lamps as the light source, e.g. [12,13], the instrument proposed herein has several advantages. 1) The contrast for small blood volume changes is 60% higher because the narrow spectrum of the LED coincides with an absorption maximum of blood. Conversely, in commercial instruments used for video acquisition, a tungsten halogen lamp is used as the light source and the green channel of the SLR cameras as the detector. Hence, parts of the spectrum that are only marginally influenced by the light absorption of the blood reduce the contrast. 2) The intensity of illumination is significantly reduced because the selection of the wavelength is performed in the illumination beam pathway and not in the imaging beam pathway. In fundus camera-based systems, the fundus is illuminated with the entire spectrum and only a relatively small range of the spectrum contributes to the changing light absorption. 3) Digital SLR cameras have a nonlinear transfer function that is optimized for color photography, not for quantitative measurements. There is no proportional relationship between light input and the resulting image intensity. Even logarithmic correction does not lead to an exact proportional relation because the transfer function is typically not described by a power law expression,  $\text{Output} = \text{Input}^\gamma$ , as it is designed for the “gamma correction” of computer monitors. Due to the non-proportional relationship, the calculated light attenuation depends on the light intensity. 4) The spectrum of tungsten lamps changes if the brightness is changed, e.g., for setting the image intensity. For quantitative evaluation (comparison of subjects, repeated measurements of the same subject), the tungsten lamp must be used at a fixed intensity level. 5) Over the data acquisition time of 10 s, an internal fixation ensures more stable fixation compared to external fixation with the contralateral eye.

It must be noted that the presented examples demonstrate the unique characteristics of the instrument and possible clinical applications; however, no conclusions should be drawn from the limited sample size. In the future, this instrument will be applied in a clinical study to assess normal values of different parameters (PAA, pulse form, and time shift) in a larger population to compare the results from patients with the results from normal subjects. It will also include other clinical parameters such as visual field, nerve fiber layer thickness, IOP, and the condition of the carotid arteries.

## 5. Conclusion

Because of the narrow band light source with a wavelength close to the peak of the blood extinction, proportional transfer function, internal fixation, and robust registration software, cardiac cycle-induced light attenuation changes caused by pulsatile changing blood volume can be quantitatively measured at any area of interest within the field of view of the video sequences. The parallel acquisition allows precise comparison of the parameters of pulsatile absorption changes and determination of the time shift between both eyes. The developed instrument is small, can function on battery power, and is low-cost and easy to use. It will be applied in a clinical study to determine the correlations of the new parameters, PAA, amplitude, and time shift with diseases such as glaucoma and stenosis of the carotid arteries.

## Funding

Deutsche Forschungsgemeinschaft DFG ((RPT) TO 115/3-1).



## Acknowledgment

We thank Robert Lämmer, Bettina Hohberger, Christian Mardin, and Folkert Horn for clinical support.

## Disclosures

RPT (P)

## References

1. D. K. Beintema, G. A. Mook, and J. G. F. Worst, "Recording of Arm-to-Retina Circulation-Time by Means of Fundus Reflectometry," *Ophthalmologica* **148**(3), 163–168 (1964).
2. H. Matsuo, F. Kogure, and K. Takahasi, "Studies of the photoelectric plethysmogram of the eye," *Proceedings XX Int. Congr. Ophthalmol.* 1966 178–182 (1966).
3. J. V. Lovasik, M. Gagnon, and H. Kergoat, "A novel noninvasive videographic method for quantifying changes in the chromaticity of the optic nerve head with changes in the intraocular pressure, pulsatile choroidal blood flow and visual neural function in humans," *Surv. Ophthalmol.* **38**(Suppl), S35–S51 (1994).
4. C. Lawrence and W. A. Schlegel, "Ophthalmic pulse studies. I. Influence of intraocular pressure," *Invest. Ophthalmol.* **5**(5), 515–525 (1966).
5. M. Best, "Carotid hemodynamics and the ocular pulse in carotid stenosis," *Neurology* **21**(10), 982–990 (1971).
6. R. P. Tornow, O. Kopp, and B. Schultheiss, "Time Course of Fundus Reflection Changes According to the Cardiac Cycle," *Invest. Ophthalmol. Vis. Sci.* **44**, 1296 (2003).
7. R. P. Tornow and O. Kopp, "Time Course and Frequency Spectrum (0 to 12.5 Hz) of Fundus Reflection," *Invest. Ophthalmol. Vis. Sci.* **47**, 3753 (2006).
8. W. H. Morgan, C. R. P. Lind, S. Kain, N. Fatehee, A. Bala, and D. Y. Yu, "Retinal vein pulsation is in phase with intracranial pressure and not intraocular pressure," *Invest. Ophthalmol. Vis. Sci.* **53**(8), 4676–4681 (2012).
9. P. B. Knecht, M. Menghini, L. M. Bachmann, R. W. Baumgartner, and K. Landau, "The ocular pulse amplitude as a noninvasive parameter for carotid artery stenosis screening: A test accuracy study," *Ophthalmology* **119**(6), 1244–1249 (2012).
10. G. Garhofer, C. Zawinka, H. Resch, K. H. Huemer, L. Schmetterer, and G. T. Dorner, "Response of retinal vessel diameters to flicker stimulation in patients with early open angle glaucoma," *J. Glaucoma* **13**(4), 340–344 (2004).
11. G. Garhofer, T. Bek, A. G. Boehm, D. Gherghel, J. Grunwald, P. Jeppesen, H. Kergoat, K. Kotliar, I. Lanzl, J. V. Lovasik, E. Nagel, W. Vilser, S. Orgul, and L. Schmetterer, "Use of the retinal vessel analyzer in ocular blood flow research," *Acta Ophthalmol.* **88**(7), 717–722 (2010).
12. W. H. Morgan, M. L. Hazelton, B. D. Betz-Stablein, D. Y. Yu, C. R. Lind, V. Ravichandran, and P. H. House, "Photoplethysmographic measurement of various retinal vascular pulsation parameters and measurement of the venous phase delay," *Invest. Ophthalmol. Vis. Sci.* **55**(9), 5998–6006 (2014).
13. W. H. Morgan, A. Abdul-Rahman, D.-Y. Yu, M. L. Hazelton, B. Betz-Stablein, and C. R. P. Lind, "Objective Detection of Retinal Vessel Pulsation," *PLoS One* **10**(2), e0116475 (2015).
14. W. H. Morgan, M. L. Hazelton, and D.-Y. Yu, "Retinal venous pulsation: Expanding our understanding and use of this enigmatic phenomenon," *Prog. Retin. Eye Res.* **55**, 82–107 (2016).
15. B. Betz-Stablein, M. L. Hazelton, and W. H. Morgan, "Modelling retinal pulsatile blood flow from video data," *Stat. Methods Med. Res.* **27**(5), 1575–1584 (2018).
16. M. Crittin and C. E. Riva, "Functional imaging of the human papilla and peripapillary region based on flicker-induced reflectance changes," *Neurosci. Lett.* **360**(3), 141–144 (2004).
17. A. L. Williams, S. Gatla, B. E. Leiby, I. Fahmy, A. Biswas, D. M. de Barros, R. Ramakrishnan, S. Bhardwaj, C. Wright, S. Dubey, J. F. Lynch, A. Bayer, R. Khandelwal, P. Ichhpujani, M. Gheith, G. Siam, R. M. Feldman, J. D. Henderer, and G. L. Spaeth, "The value of intraocular pressure asymmetry in diagnosing glaucoma," *J. Glaucoma* **22**(3), 215–218 (2013).
18. M. Sullivan-Mee, C. C. Ruegg, D. Pensyl, K. Halverson, and C. Qualls, "Diagnostic precision of retinal nerve fiber layer and macular thickness asymmetry parameters for identifying early primary open-angle glaucoma," *Am. J. Ophthalmol.* **156**(3), 567–577.e1 (2013).
19. J. M. S. De Leon, C. Y. Cheung, T.-Y. Wong, X. Li, H. Hamzah, T. Aung, and D. H. Su, "Retinal vascular caliber between eyes with asymmetric glaucoma," *Graefes Arch. Clin. Exp. Ophthalmol.* **253**(4), 583–589 (2015).
20. A. A. K. Fansi, H. Boisjoly, M. Chagnon, and P. J. Harasymowycz, "Comparison of different methods of inter-eye asymmetry of rim area and disc area analysis," *Eye (Lond.)* **25**(12), 1590–1597 (2011).
21. S. Trokel, "Photometric Study of Ocular Blood Flow in Man," *Arch. Ophthalmol.* **71**(4), 528–530 (1964).
22. R. P. Tornow, R. Kolář, and J. Odstrčilík, "Non-mydratric video ophthalmoscope to measure fast temporal changes of the human retina," in *Progress in Biomedical Optics and Imaging - Proc. SPIE* **9540**, 954006 (2015).
23. N. Bosschaart, G. J. Edelman, M. C. G. Aalders, T. G. van Leeuwen, and D. J. Faber, "A literature review and novel theoretical approach on the optical properties of whole blood," *Lasers Med. Sci.* **29**(2), 453–479 (2014).
24. F. C. Delori and K. P. Pflibsen, "Spectral reflectance of the human ocular fundus," *Appl. Opt.* **28**(6), 1061–1077

- (1989).
25. J. Jiang, D. Liu, J. Gu, and S. Susstrunk, "What is the space of spectral sensitivity functions for digital color cameras?" in *2013 IEEE Workshop on Applications of Computer Vision (WACV)* (IEEE, 2013), pp. 168–179.
  26. D. Sliney, D. Aron-Rosa, F. DeLori, F. Fankhauser, R. Landry, M. Mainster, J. Marshall, B. Rassow, B. Stuck, S. Trokel, T. M. West, and M. Wolffe, "Adjustment of guidelines for exposure of the eye to optical radiation from ocular instruments: statement from a task group of the International Commission on Non-Ionizing Radiation Protection (ICNIRP)," *Appl. Opt.* **44**(11), 2162–2176 (2005).
  27. R. P. Tornow, A. Milczarek, J. Odstrcilik, and R. Kolar, "Binocular video ophthalmoscope for simultaneous recording of sequences of the human retina to compare dynamic parameters," in *Progress in Biomedical Optics and Imaging - Proceedings of SPIE* (2017), Vol. 10413.
  28. R. Kolar, R. P. Tornow, J. Odstrcilik, and I. Liberdova, "Registration of retinal sequences from new video-ophthalmoscopic camera," *Biomed. Eng. Online* **15**(1), 57 (2016).
  29. B. D. Lucas and T. Kanade, "An Iterative Image Registration Technique with an Application to Stereo Vision.," in *Proceedings of the 7th International Joint Conference on Artificial Intelligence* (1981), pp. 674–679.
  30. R. Kolar, R. P. Tornow, and J. Odstrcilik, "Retinal image registration for eye movement estimation," in *2015 37th Annual International Conference of the IEEE Engineering in Medicine and Biology Society (EMBC)* (IEEE, 2015), Vol. 2015–Novem, pp. 5247–5250.
  31. F. Lauterwald, C. P. Neumann, R. Lenz, A. G. Juenemann, C. Y. Mardin, K. Meyer-Wegener, and F. K. Horn, "The Erlangen Glaucoma Registry: a Scientific Database for Longitudinal Analysis of Glaucoma," *Tech. reports / Dep. Inform.* (ISSN 2191–5008) **CS-2011**, **2**, 1–9 (2012).
  32. F. K. Horn, C. Y. Mardin, R. Laemmer, D. Baleanu, A. M. Juenemann, F. E. Kruse, and R. P. Tornow, "Correlation between local glaucomatous visual field defects and loss of nerve fiber layer thickness measured with polarimetry and spectral domain OCT," *Invest. Ophthalmol. Vis. Sci.* **50**(5), 1971–1977 (2009).
  33. D. Bendschneider, R. P. Tornow, F. K. Horn, R. Laemmer, C. W. Roessler, A. G. Juenemann, F. E. Kruse, C. Y. Mardin, D. Bendschneider, R. P. Tornow, F. K. Horn, R. Laemmer, C. W. Roessler, A. G. Juenemann, F. E. Kruse, and C. Y. Mardin, "Retinal nerve fiber layer thickness in normals measured by spectral domain OCT," *J. Glaucoma* **19**(7), 475–482 (2010).
  34. A. A. Kamshilin, E. Nippolainen, I. S. Sidorov, P. V. Vasilev, N. P. Erofeev, N. P. Podolian, and R. V. Romashko, "A new look at the essence of the imaging photoplethysmography," *Sci. Rep.* **5**(1), 10494 (2015).
  35. T. Mase, A. Ishibazawa, T. Nagaoka, H. Yokota, and A. Yoshida, "Radial peripapillary capillary network visualized using wide-field montage optical coherence tomography angiography," *Invest. Ophthalmol. Vis. Sci.* **57**(9), OCT504 (2016).
  36. C. Lommatzsch, K. Rothaus, J. M. Koch, C. Heinz, and S. Grisanti, "Vessel density in OCT angiography permits differentiation between normal and glaucomatous optic nerve heads," *Int. J. Ophthalmol.* **11**(5), 835–843 (2018).
  37. Y. Yokoyama, N. Aizawa, N. Chiba, K. Omodaka, M. Nakamura, T. Otomo, S. Yokokura, N. Fuse, and T. Nakazawa, "Significant correlations between optic nerve head microcirculation and visual field defects and nerve fiber layer loss in glaucoma patients with myopic glaucomatous disk," *Clin. Ophthalmol.* **5**, 1721–1727 (2011).
  38. A. S. Mursch-Edlmayr, N. Luft, D. Podkowinski, M. Ring, L. Schmetterer, and M. Bolz, "Laser speckle flowgraphy derived characteristics of optic nerve head perfusion in normal tension glaucoma and healthy individuals: a Pilot study," *Sci. Rep.* **8**(1), 5343 (2018).
  39. R. W. Knighton, C. Baverez, and A. Bhattacharya, "The directional reflectance of the retinal nerve fiber layer of the toad," *Invest. Ophthalmol. Vis. Sci.* **33**(9), 2603–2611 (1992).
  40. X.-R. Huang, R. W. Knighton, W. J. Feuer, and J. Qiao, "Retinal nerve fiber layer reflectometry must consider directional reflectance," *Biomed. Opt. Express* **7**(1), 22–33 (2016).
  41. A. Wartak, M. Augustin, R. Haindl, F. Beer, M. Salas, M. Laslandes, B. Baumann, M. Pircher, and C. K. Hitzenberger, "Multi-directional optical coherence tomography for retinal imaging," *Biomed. Opt. Express* **8**(12), 5560–5578 (2017).
  42. L. An, J. Chao, M. Johnstone, and R. K. Wang, "Noninvasive imaging of pulsatile movements of the optic nerve head in normal human subjects using phase-sensitive spectral domain optical coherence tomography," *Opt. Lett.* **38**(9), 1512–1514 (2013).
  43. H. Spahr, D. Hillmann, C. Hain, C. Pfäffle, H. Sudkamp, G. Franke, and G. Hüttmann, "Imaging pulse wave propagation in human retinal vessels using full-field swept-source optical coherence tomography," *Opt. Lett.* **40**(20), 4771–4774 (2015).
  44. L. Schmetterer, S. Dallinger, O. Findl, H. G. Eichler, and M. Wolzt, "A comparison between laser interferometric measurement of fundus pulsation and pneumotonometric measurement of pulsatile ocular blood flow. 1. Baseline considerations," *Eye (Lond.)* **14**(1), 39–45 (2000).
  45. A. Arthur, A. Alexander, S. Bal, A. Sivadasan, and S. Aaron, "Ophthalmic masquerades of the atherosclerotic carotids," *Indian J. Ophthalmol.* **62**(4), 472–476 (2014).
  46. E. A. Choromokos, L. A. Raymond, and J. G. Sacks, "Recognition of Carotid Stenosis with Bilateral Simultaneous Retinal Fluorescein Angiography," *Ophthalmology* **89**(10), 1146–1148 (1982).
  47. F. Moret, C. M. Reiff, W. A. Lagrèze, and M. Bach, "Quantitative Analysis of Fundus-Image Sequences Reveals Phase of Spontaneous Venous Pulsations," *Transl. Vis. Sci. Technol.* **4**(5), 3 (2015).